Supplementary Figure 1. Generation of *Vglut3-Cre* mice

A

Cre-recombinase

BAC RP24-88H21 (167 kb)

VGLUT3 (Slc17a8)

B

GFP

Vglut3

C

E

D
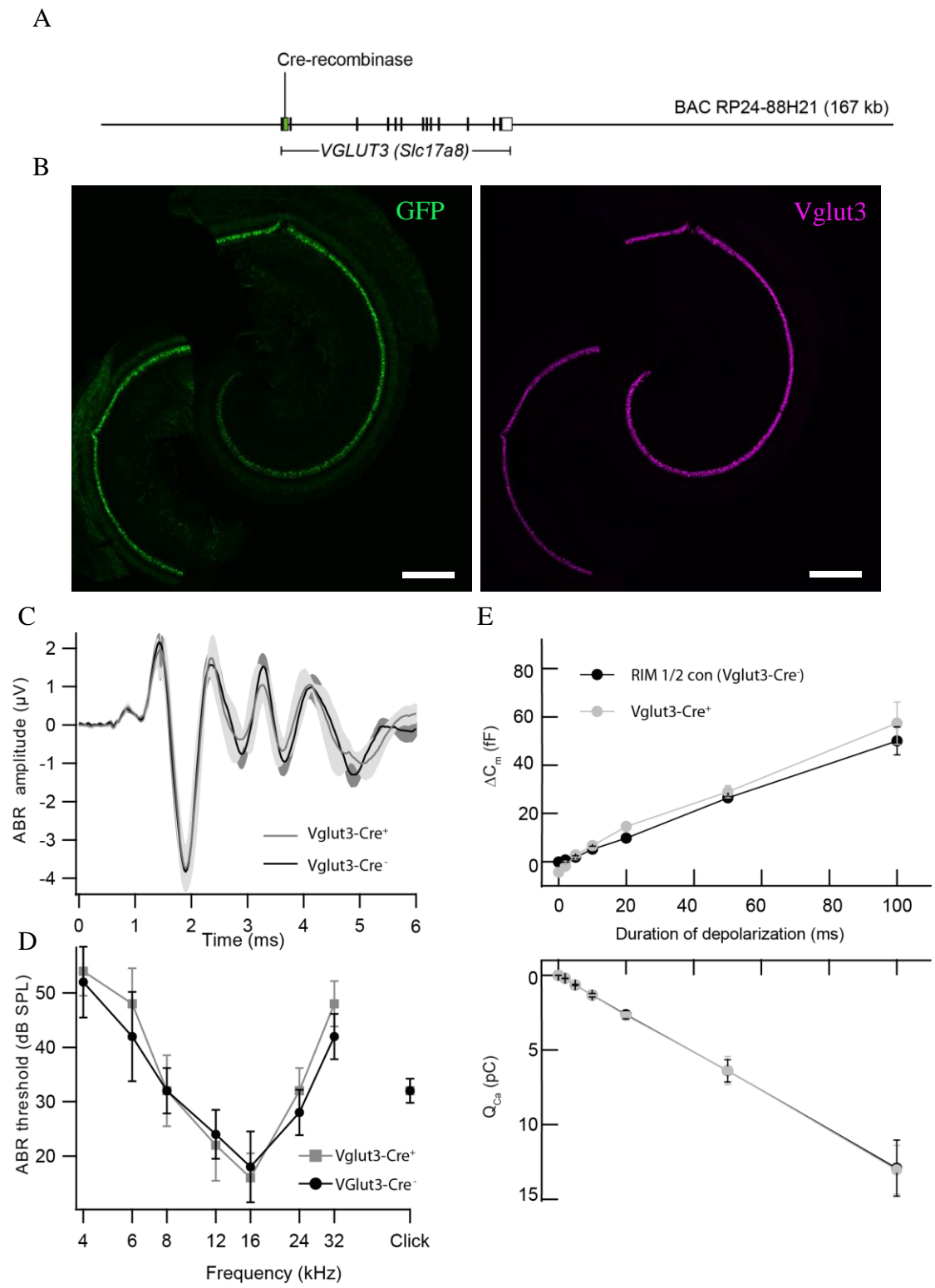
(**A**) For hair cell-specific Cre-recombination we generated a *Vglut3-Cre* BAC transgene. The Cre-coding sequence (green bar in the schematic representation) was inserted into BAC RP24-88H21, into the start codon of the *Vglut3*/*Slc17a8* gene, thus placing the expression of Cre under the control of the *Vglut3* promoter. Although the rest of the *Vglut3* gene was left intact (black bars represent the exons, the white bar the 3' UTR), it lacks a functional start codon and should therefore not be expressed from the *Vglut3-Cre* BAC transgene.

(**B**) Acutely dissected cochlea of mice at postnatal days 14 (p14) demonstrating *Vglut3*-driven Cre-recombination in IHCs and OHCs as reported by a floxed EGFP reporter (SI Appendix ref. 1). Left panel shows GFP fluorescence (green), indicating Cre activity, right panel shows immunohistochemical staining against Vglut3 (magenta). In addition, some Cre-expression was found in capillaries. Scale bar, 200 μm.

(**C**) Grand averages of ABR waveforms in response to 80 dB Click stimulation from Vglut3-Cre positive (grey, n = 5) and Vglut3-Cre negative (black, n = 5) mice. No significant differences in ABR amplitudes or latencies were found.

(**D**) ABR thresholds from Vglut3-Cre positive (grey, n = 5) and Vglut3-Cre negative (black, n = 5) mice were comparable.

(**E**) Average ΔC_m (upper panel) of p14-16 RIM1/2 con IHCs (black, number of cell, n = 10, number of animal, N = 4, Vglut3-Cre$^-$) and Vglut3-Cre$^+$ IHCs (grey, n = 3, N = 3) and corresponding Ca^{2+} current integral (Q_{Ca}, lower panel) for depolarizations of different durations.

**Supplementary Figure 2: RIM mRNA analysis in IHCs and the organ of Corti**
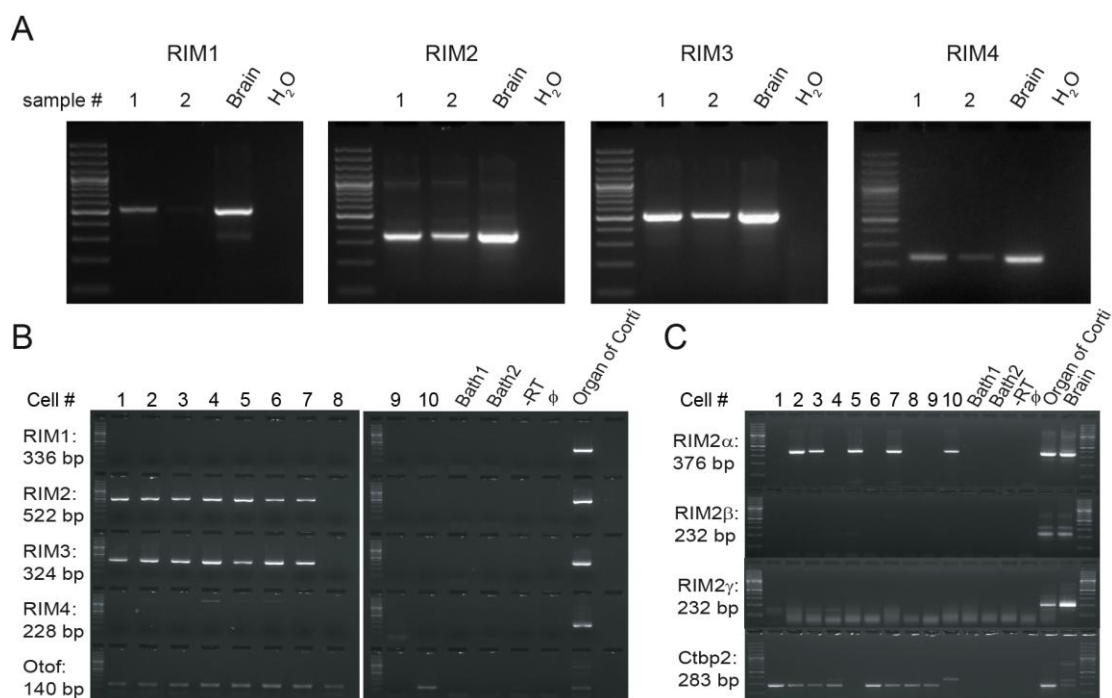
(**A**) Organ of Corti RT-PCR for RIM1-4: all 4 RIM genes are expressed in the organ of Corti of hearing C57Bl/6 mice (postnatal days 14-16, also for B and C, see also supplementary methods). Primers were designed to recognize all RIM1 and RIM2 isoforms, brain cDNA served as positive control, H_2O as negative control.

(**B**) Nested RT-PCR from single IHCs for RIM1-4: only RIM2 and 3 are expressed in most IHCs. Otoferlin served as the positive control, bath solution aspirated close to hair cells (Bath1, Bath2) as well as one IHC without reverse transcriptase treatment (-RT) and H_2O (ϕ) as negative controls.

(**C**) RIM2 isoform specific, nested RT-PCR on single IHCs. RIM2α was positive in most cells RIM2β and RIM2γ were less frequently detected. CtBP2 served as the positive control for IHC identity, brain cDNA as positive control for the reaction, negative controls were as above.

Supplementary Figure 3: RIM3γ but not RIM1 is present at IHC AZs

A

B
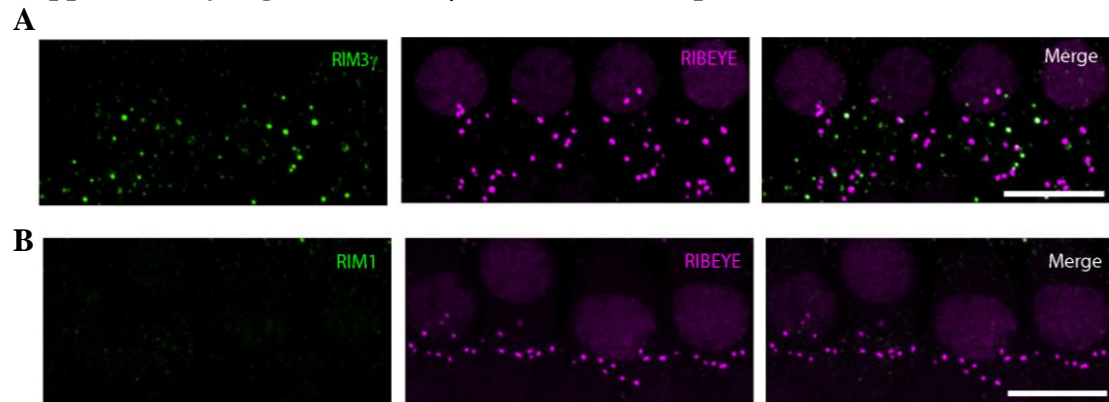
(**A**) Projections of confocal sections of a wild-type organ of Corti (n = 4) immunolabeled with a RIM3γ-specific antibody (green, left and right panel) and a CtBP2/RIBEYE antibody labeling the presynaptic ribbons (magenta, middle and right panel) and IHC nuclei. Note green RIM3γ immunofluorescence at the ribbon-type AZs of IHCs. Scale bar: 10 µm.

(**B**) Projections of confocal sections of a wild type organ of Corti (n = 4) immunolabeled with a RIM1-specific antibody (green, left and right panels) and a CtBP2/RIBEYE antibody labeling the presynaptic ribbon (magenta, middle and right panels) and IHC nuclei. None of the ribbons showed RIM1-immunofluorescence, indicating the absence of RIM1 from the ribbon-type AZ of IHCs. Scale bars, 10 µm.

Supplementary Figure 4: Voltage-dependence and kinetics of I_{Ca} activation as well as I_{Ca} inactivation are unaltered in RIM2α SKO IHCs
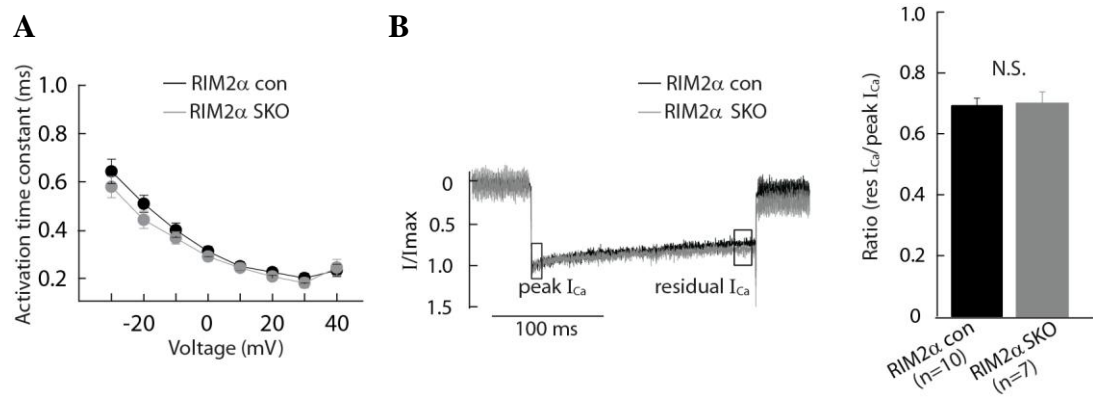
(**A**) The average time constant of activation of the Ca^{2+} currents elicited by 10 ms step depolarization obtained from exponential fitting from zero-crossing of current until 2 ms of depolarization depolarization was not different between RIM2α SKO (grey, number of cell, n = 15, number of animal, N = 3) and RIM2α con (black, n = 10, N = 3).

(**B**) Representative Ca^{2+} current (left) and mean Ca^{2+} current inactivation (right) estimated as the ratio of residual to peak Ca^{2+} current for 200 ms long depolarization: comparable extent of inactivation for Ca^{2+} currents of p14-18 RIM2α SKO (grey, n = 7, N = 3) and RIM2α con (black, n = 10, N = 3) IHCs (res I_{Ca}/ peak I_{Ca}= 0.69 ± 0.04 vs. 0.69 ± 0.02, p = 0.8). Values are presented as mean ± SEM.

Supplementary Figure 5: Reduced synaptic Ca^{2+} influx in RIM2-deficient IHCs
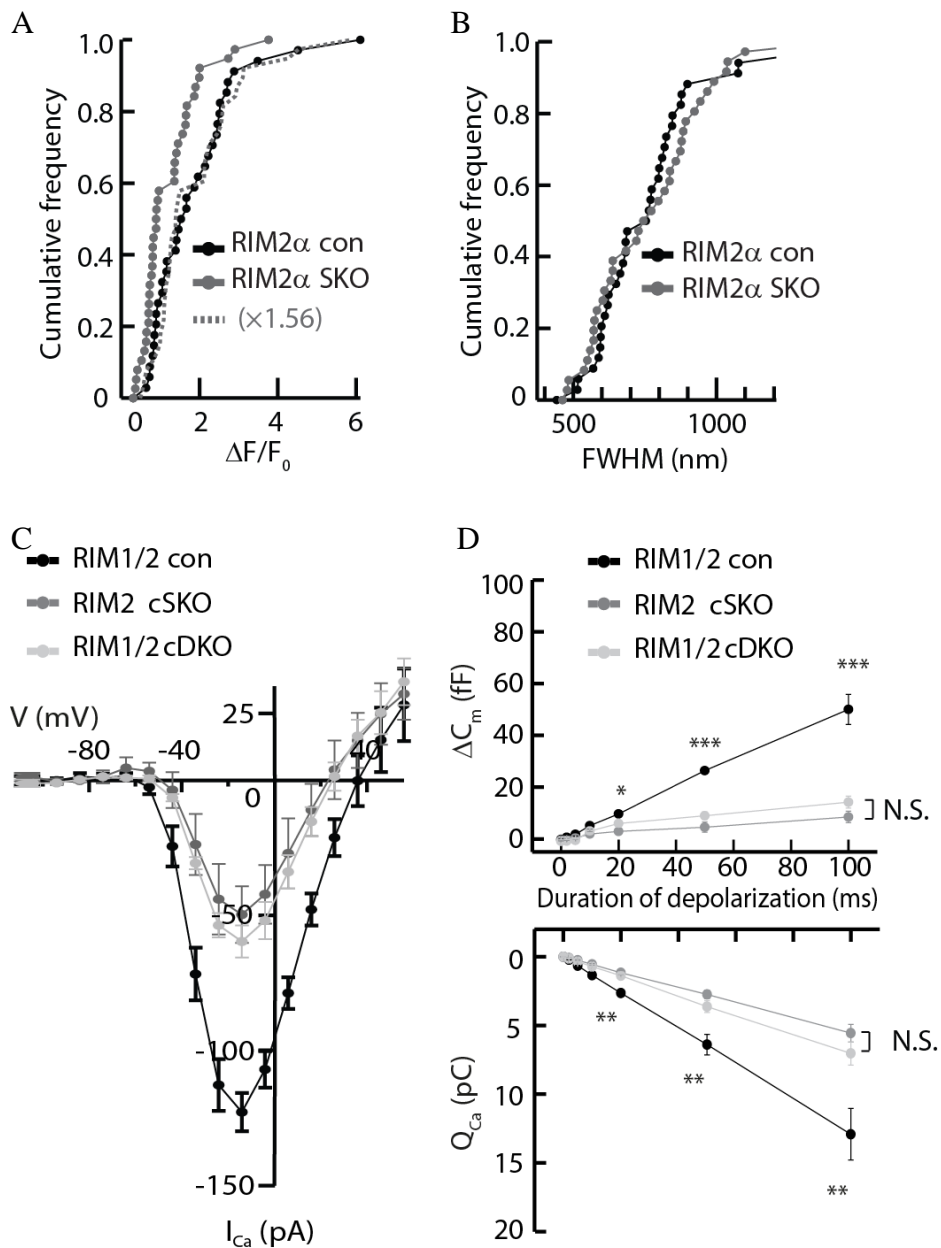

(A) $\Delta F/F_0$ and **(B)** Full-width-at-half-maximum (FWHM) of ΔF obtained from Gaussian fits (see Figure 4C) plotted as a cumulative distribution for RIM2α SKO AZs (grey, 40 AZs in 13 IHCs in 7 organs) and RIM2α con AZs (black, 35 AZs in 15 IHCs in 7 organs). Dotted line represents the RIM2α SKO data scaled by 1.56.

(C) Average steady-state I_{Ca}-V of RIM1/2 cDKO (light grey, number of cell, n = 8, number of animal, N = 5), RIM2 cSKO (dark grey, n = 7, N = 4), and RIM1/2 con

(black, n = 10, N = 4) IHCs acquired with 10 ms long depolarizations (steady-state Ca^{2+} current during depolarization): comparable peak I_{Ca} from RIM1/2 cDKO and RIM2 cSKO (p = 0.2) but significantly different peak I_{Ca} from RIM1/2 con (p < 0.001 in both genotypes).

(D) Average ΔC_m (upper panel) of p14-16 RIM1/2 con IHCs (black, n = 10, N = 4) RIM1/2 cDKO IHCs (light grey, n = 7, N = 4) and RIM2 cSKO IHCs (dark grey, n = 7, N = 4) and corresponding Ca^{2+} current integral (Q_{Ca}, lower panel) for depolarizations of different durations: comparable Q_{Ca} from RIM1/2 cDKO and RIM2 cSKO (N.S.)

Supplementary Figure 6: Criteria for and quantification of tether length in the ribbon synapse

A

C

B
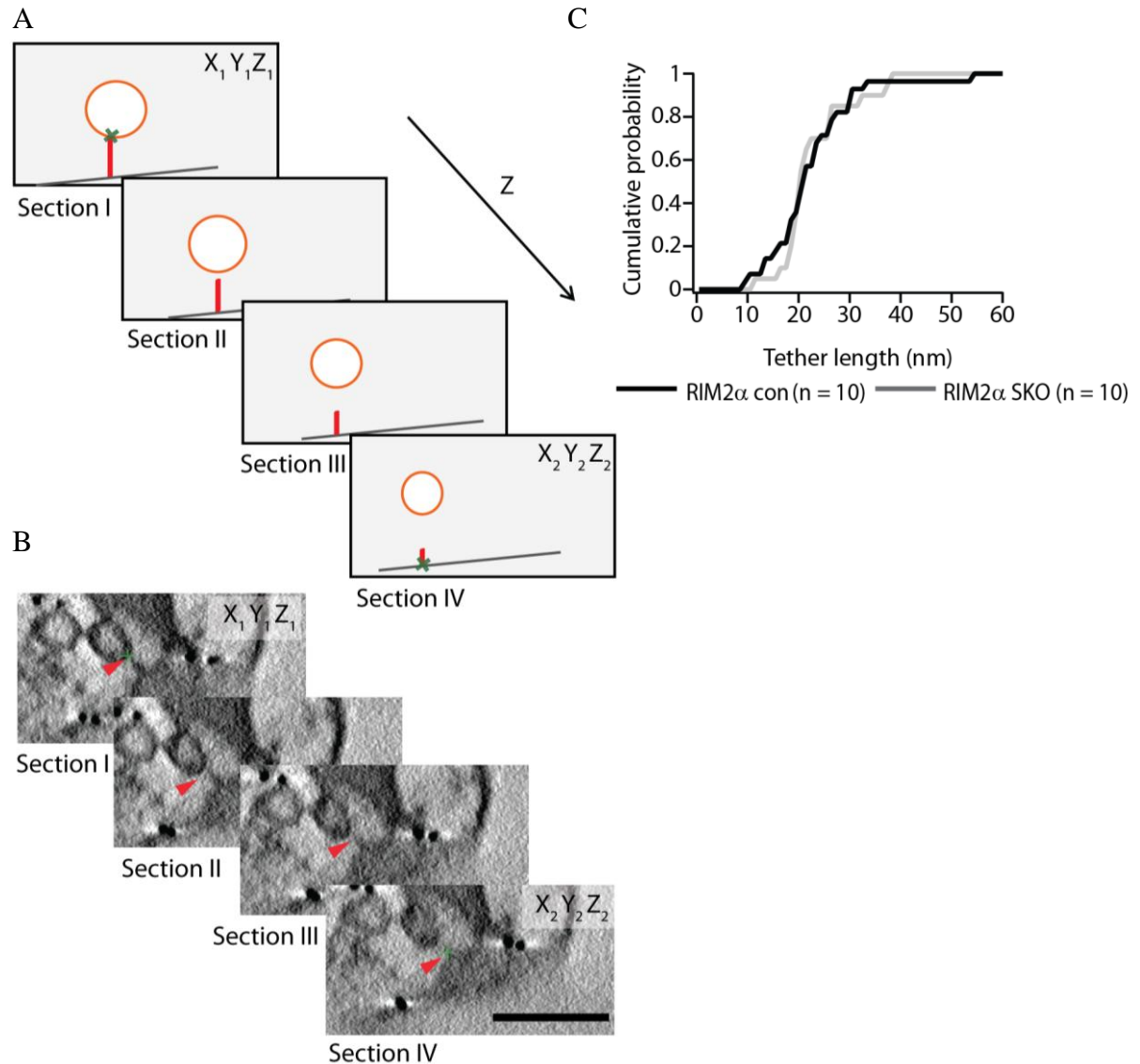
(A) Illustration of single tether as it is observed in consecutive virtual electron tomographic sections I, II, III, and IV (not drawn to scale). Tether starting coordinates are X_1, Y_1, Z_1 in section I and ending coordinates are X_2, Y_2, Z_2 in section IV (green cross in section I and IV). Tether length is calculated according to the equation: *Tether Length = $\sqrt{((X_2-X_1)^2 + (Y_2-Y_1)^2 + (Z_2-Z_1)^2)}$*. **(B)** Exemplary consecutive virtual electron tomographic sections of RIM2α con depicting one single tethered synaptic vesicle in the membrane-proximal pool. The tether is indicated by red arrowheads and

tether coordinates by the green cross in section I and IV. Scale bar, 100 nm. **(C)** Graph representing the cumulative probability distribution of tethers vs. tether length. The average tether length in the membrane-proximal pool is unaltered in RIM2α SKO IHCs (grey, number of tomogram, n = 10) compared to wild-type littermates RIM2α con (black, n = 10, p = 1).

Supplementary Figure 7: RIM2α SKO mice show otoacoustic emissions but increased ABR latency - normal ABRs in RIM1α SKO
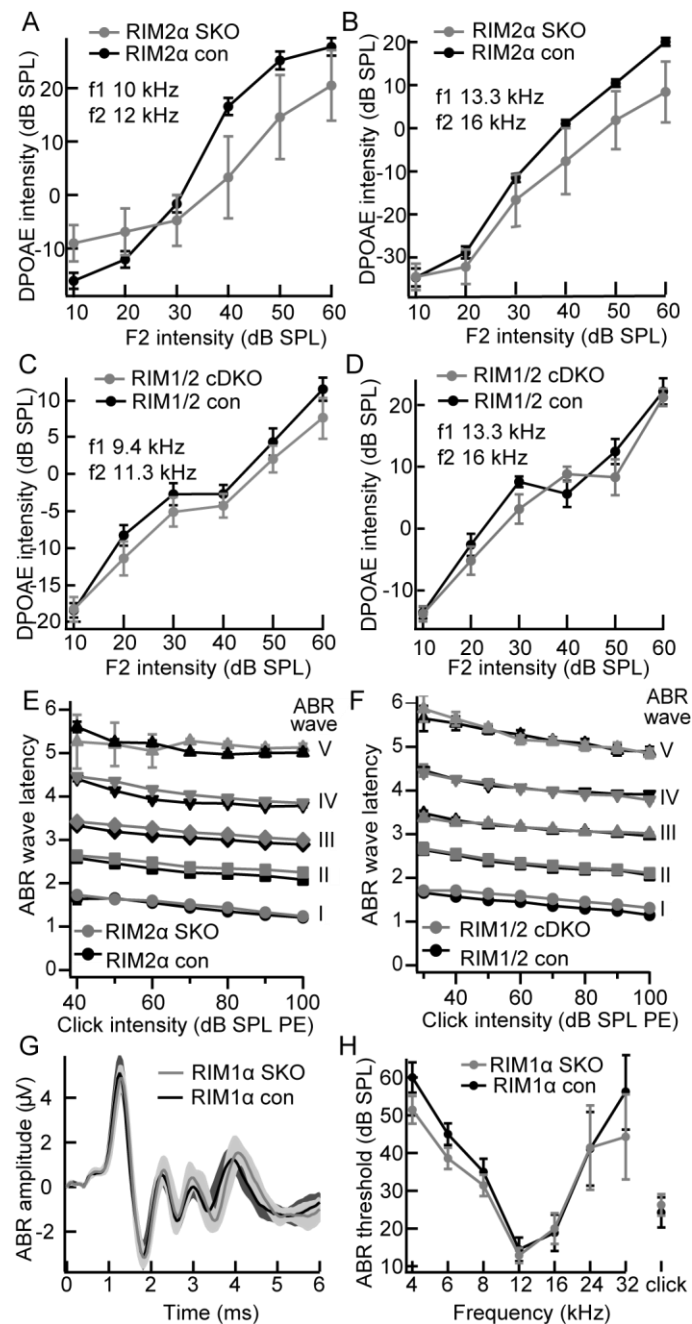
(**A-B**) DPOAE growth function of RIM2α SKO (grey, n = 4) and RIM2α con (black, n = 5) mice in response to pairs of continuous tones (**A**) (frequencies f1 = 10 kHz and f2 = 12 kHz) and (**B**) (frequencies f1 = 13.3 kHz and f2 = 16 kHz) of varying

intensities. **(C-D)** same for RIM1/2 cDKO mice (grey, n = 12) and littermate controls (black, n = 10).

(E-F) Latencies of ABR waves II-V in response to click stimulation at varying intensities are significantly delayed in RIM2α SKO mice (E, grey, n = 15) compared to RIM2α con (E, black, n = 15), whereas in hair-cell specific RIM1/2 cDKO mice (E, grey, n = 8), only wave I is significantly delayed compared to littermate controls (E, black, n = 10).

(**G**) Grand averages of ABR waveforms in response to 80 dB clicks of RIM1α SKO (red, n = 9) are identical to those of RIM1α con (black, n = 7) mice.

(**H**) ABR thresholds (right) of RIM1α SKO mice (grey, n = 9) are not significantly different from those of RIM1α con mice (black, n = 7).

Supplementary Figure 8: Extracellular recordings from SGN and cochlear nucleus neurons of RIM2α SKO mice
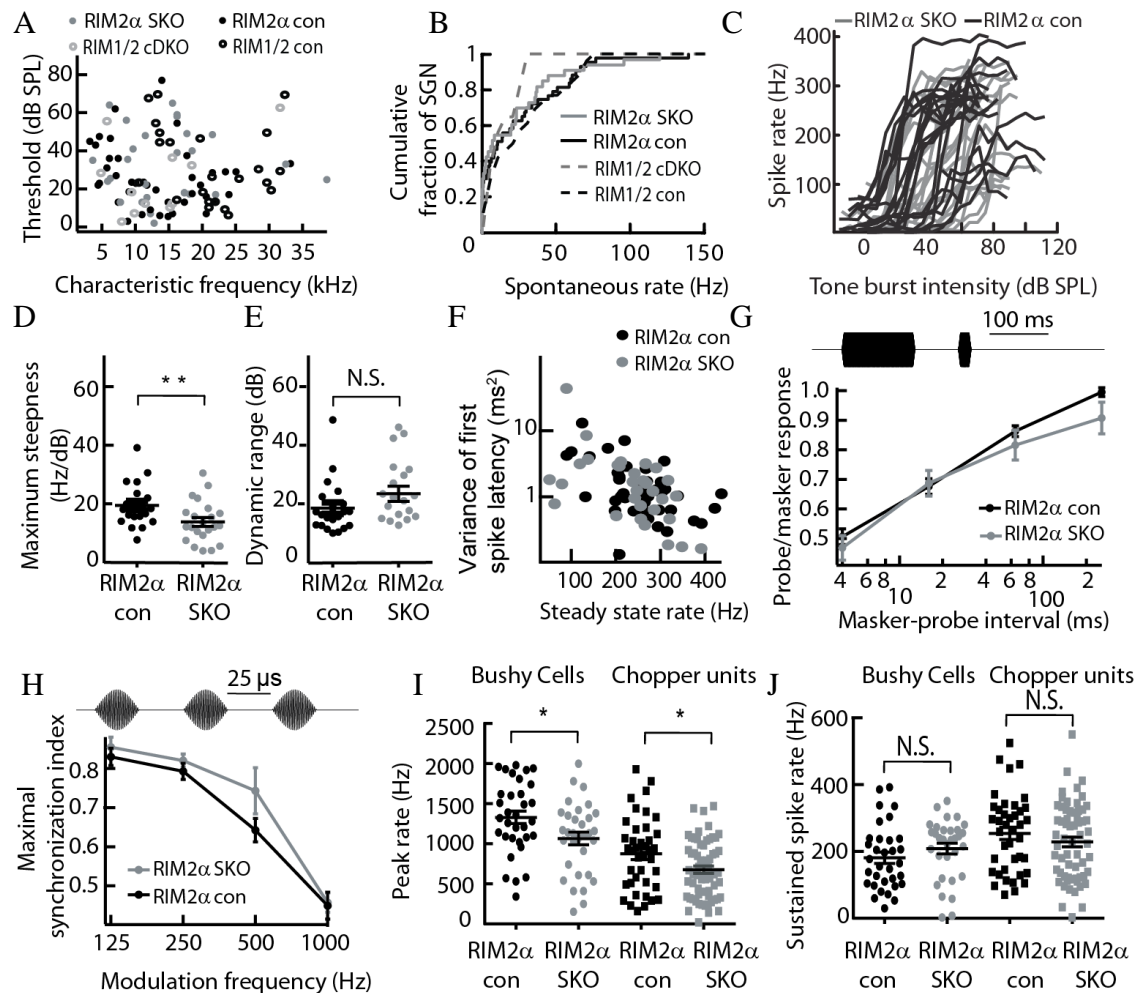
(**A**) Thresholds at the characteristic frequency of individual RIM2α SKO spiral ganglion neurons (SGNs) (black closed circles, n = 41) were comparable to those of RIM2α con SGN (grey closed circles, n = 31) and their characteristic frequencies (CFs) covered the normal frequency range. In the smaller dataset from RIM1/2 cDKO animals (grey open circles, n = 11), our sample included fewer high-frequency neurons, but thresholds in the lower frequency range were also comparable to those in RIM1/2 con animals (black open circles, n = 24).

(**B**) Spontaneous action potential rates in individual RIM2α SKO (grey line, n = 43) and RIM1/2 cDKO (grey dashed line, n = 11) SGNs tended to be lower than in RIM2α con (black line, n = 33) and RIM1/2 cDKO (black dashed line, n = 25) SGNs, respectively. However, this did not reach significance (Kolmogorov-Smirnov test).

(**C-E**) Rate increases to sound burst stimulation at varying intensities were shallower in RIM2α SKO SGNs (grey, n = 22) compared to RIM2α con SGNs (black, n = 21, p = 0.01). The maximal rate increase per dB intensity increment was significantly lower in RIM2α SKO SGNs (D) and the dynamic range over which the rate increased between 10 and 90% of the difference between spontaneous and maximal discharge rate occurs tended to be larger than in RIM2α con SGNs (E, p = 0.42).

(**F**) The spike time jitter, measured as the variance of the first spike latency in response to 50 ms tone bursts at CF co-varied with the spike rates and was not different between RIM2α SKO (grey, n = 32) and RIM2α con SGNs (black, n = 42, p = 0.51).

(**G**) Top, illustration of the stimulus paradigm for assessment of recovery from masking: a 100 ms masker pulse is followed by a silent interval of variable duration and a 15 ms probe pulse (both at CF, 30 dB above threshold). The entire cycle length is 500 ms. Bottom, the number of spikes in response to the first 10 ms of the probe as a fraction of the number of spikes in response to the first 10 ms of the masker are comparable in RIM2α SKO (grey, n = 19) and RIM2α con SGNs (black, n = 19), indicating a normal amount of masking and time course of recovery.

(**H**) Top, illustration of the stimulus paradigm for assessment of synchronicity of firing to the sound envelope of amplitude modulated tones. 3 second continuous transposed tones with CF as the carrier frequency and modulation frequencies of 125,

250, 500 and 1000 Hz were presented at varying intensities that covered the entire dynamic range of each unit. The synchronization index (or vector strength) was calculated as a measure of phase locking of spikes to the stimulus waveform. Bottom, average maximum synchronization indices for different modulation frequencies were comparable between RIM2α SKO (grey, n = 9-11) and RIM2α con SGNs (black, n = 9-12).

(**I**), (**J**) Maximal rates (**I**) at sound onset in bushy cells (primary-like post-stimulus time histogram (PSTH) but located superficially in the cochlear nucleus, or primary-like with notch pattern, circles, n = 33 each) and chopper neurons /multipolar cells of the cochlear nucleus (squares, n = 64 for RIM2α SKO, n = 40 for RIM2α con, p = 0.02) were significantly reduced in RIM2α SKO (grey) compared to RIM2α con mice (black), but sustained spiking activity (**J**) was normal.

Supplementary Table 1. RIM-primers for RT-PCR/nested RT-PCR

	fwd/rev	1st	Nested
RIM1	forward	GAGGAACGAACGAGACAGATGAAA	GTCCGCCAAGTCATCAGATAGTGA
	reverse	TTTTTAACTTCTTGTGGCCGGACT	TTCTGCTTCTTCGAGACACAATGG
RIM2	forward	GCCTCTCAACTCAGCCAAAC	GATGGCAGCATGAACAGCTA
	reverse	CAGAGACGATTGGGAAGCTC	TAGGGAGGAAGGAGGGAAGA
RIM3	forward	TGGGAGCACCAACAGTAACA	AAGCCAGTTCAGTGACTTCTGGA
	reverse	CATGTTTTCTTGGCCACCTT	GTTCTCCAGCAGGTAAGCCTTGAT
RIM4	forward	ACACTGCCAGCTGCCTATATCAAG	TGTCTGCATTGCCAAGAAGAAAAC
	reverse	CGTAGTTTCCCCACACGATTACCT	GGGACTCTCAGGAAACAGAAGCAC

Supplementary Table 2 RIM-isoform-specific primers for RT-PCR/nested RT-PCR

	fwd/rev	1st	nested
RIM1α	forward	CTCCCCCTATGCAAGAACTG	ACCGAGGAGGAGAGGAACAT
	reverse	GACCTTGATCGCTCTTGGAG	TTGTTCGATCGCAGAGACAC
RIM1β	forward	CAGAAGCTGTCCCATTTTCC	CCTTCTGGAGCTTTCTGAGC
	reverse	GACCTTGATCGCTCTTGGAG	TTGTTCGATCGCAGAGACAC
RIM2α	forward	AGCAAGAGCAGAAGGGTGAT	CTGCAGCAACCTGATCAAAA
	reverse	TCCACATCTTCATCATCCACA	ATTGAGGCTCACGCTGAGAT
RIM2β	forward	GCCAGGTCTGCAATTCTGTT	CGCTGAACAATGCAAGAAAA
	reverse	TCCACATCTTCATCATCCACA	ATTGAGGCTCACGCTGAGAT
RIM2γ	forward	TCCATGCAGCGCTCTCAG	CAGCCTCTCTGCCTCTTTTG
	reverse	TAGCTGTTCATGCTGCCATC/ TCCAGGAAATCACTGAACTGG	CCTCCTCCTTCTCCTTCATCT

Supplementary Table 3. Number of Ca^{2+} channels, single channel current, and maximum open probability as estimated by non-stationary fluctuation analysis

	RIM2α con (n = 7, N = 3)	RIM2α SKO (n = 8, N = 3)	p value
Number of Ca^{2+} channels N	1342 ± 65	1102 ± 72	0.02*
Single channel current i (pA)	0.73 ± 0.02	0.79 ± 0.02	0.056
Maximum open probability p	0.69 ± 0.01	0.72 ± 0.04	0.485

Data were obtained from parabolic fits to variance-mean relationships obtained from ensembles of Ca^{2+} tail currents as shown in Figure 3B. Values are presented as mean ± SEM.

Supplementary experimental procedures

RT-PCR and single-cell nested RT-PCR

Wild-type C57Bl/6 mice at the age of postnatal days (p) 14 through 16 were used in this study to determine the general expression of RIMs in the organ of Corti and in single IHCs.

For RT-PCR of organs of Corti we isolated total RNA from preparations of the organ of Corti of 2 week-old mice using TRIzolReagent (Invitrogen). Reverse transcription was performed with SuperScriptII Rt according to the manufacturer's instructions using oligo dt primers. Sequences of RIM-specific primers are listed in Table 1 and only the first PCR was run with less than 30 cycles.

Individual IHCs from the apical coils of freshly dissected organs of Corti were harvested after cleaning off supporting cells at a high bath perfusion rate (3 ml/min). 11 IHCs were collected at each trial. 10 cells were used for checking the expression of each RIM isoform and 1 IHC was used as negative control by omitting the Reverse Transcriptase from the reaction. Each individual IHC was aspirated and the pipette content was transferred into first strand cDNA synthesis mix containing after the dilution: 50 mM Tris-HCl, pH 8.3, 75 mM KCl, 5 mM $MgCl_2$, 5 mM DTT, 100 units of SuperScript II Reverse Transcriptase (Invitrogen, Carlsbad, CA) and 40 units RNaseOUT Ribonuclease inhibitor (Invitrogen). Reverse transcription was performed with oligo (dT) primers according to the manufacturer's instructions. Aspirated bath solution was used as a negative control. Each cDNA mix was used as a template for two subsequent PCR reactions with nested primers specific for RIM1α-β, RIM2α-γ, RIM3γ, RIM4γ, and otoferlin or CtBP2 (specific) cDNA. Primer sequences are listed

in Tables 1 and 2. Single-cell nested RT-PCR was performed 4 times and 5 times in checking the RIM 1-4 expression and RIM2 isoforms, respectively.

Non-stationary fluctuation analysis

Non-stationary fluctuation analysis of Ca^{2+} tail currents was performed as described previously (SI Appendix ref. 2). Briefly, Ca^{2+} tail currents were recorded at a membrane potential of -64 mV and 520 sweeps per ensemble were acquired with an inter-sweep interval of 80 ms. Variance of Ca^{2+} tail currents was estimated as the average of squared differences between pairs of consecutive responses in order to reduce the contribution of capacitive currents and current run-down to the total variance. Tail current variance was plotted versus mean current and fitted with the following equation: Eq.1. $var = i \times I_{mean} - (I^2_{mean}/N) + offset$

The number of Ca^{2+} channels (N) and the single channel current (i) were estimated using Eq.1. The maximum open probability (p_o) was estimated using the following equation: Eq.2. $p_o = I_{mean,max}/(N \times i)$

References

1. Nakamura T, Colbert MC, Robbins J (2006) Neural crest cells retain multipotential characteristics in the developing valves and label the cardiac conduction system. *Circ Res* 98(12):1547–1554.

2. Frank T, Khimich D, Neef A, Moser T (2009) Mechanisms contributing to synaptic Ca2+ signals and their heterogeneity in hair cells. *Proc Natl Acad Sci U S A* 106(11):4483-4488.